RESEARCH ARTICLE
SPACE PHYSICS: MAGNETOSPHERIC PHYSICS

Earth and Planetary Physics
6: 563–575, 2022
doi: 10.26464/epp2022050

Simultaneous occurrence of four magnetospheric wave modes and the resultant combined scattering effect on radiation belt electrons

YiWen Zhao[1], Zheng Xiang[1*], XuDong Gu[1*], BinBin Ni[1,2], Xin Ma[1], YueQun Lou[3], LuHuai Jiao[1], RuoXian Zhou[1], DeYu Guo[1], YangXiZi Liu[1], and JunHu Dong[1]

[1]Department of Space Physics, School of Electronic Information, Wuhan University, Wuhan 430072, China;

[2]Chinese Academy of Sciences Center for Excellence in Comparative Planetology, Hefei 230026, China;

[3]Institute of Space Science and Applied Technology, Harbin Institute of Technology, Shenzhen 518005, China

Key Points:

- Electron cyclotron harmonic waves, exohiss, magnetosonic waves, and electromagnetic ion cyclotron waves are reported to occur simultaneously on the duskside at $L \approx 5.0$.
- The combined electron scattering effect of the four wave modes is investigated in detail.
- The coexistence of multiple wave modes tends to affect—in combination or individually—the radiation belt electron distributions at different energy ranges.

Citation: Zhao, Y. W., Xiang, Z., Gu, X. D., Ni, B. B., Ma, X., Lou, Y. Q., Jiao, L. H., Zhou, R. X., Guo, D. Y., Liu, Y. X. Z., and Dong, J. H. (2022). Simultaneous occurrence of four magnetospheric wave modes and the resultant combined scattering effect on radiation belt electrons. *Earth Planet. Phys.*, *6*(6), 563–575. http://doi.org/10.26464/epp2022050

Abstract: We report a representative concurrent event of four wave modes at $L \approx 5.0$, including electrostatic electron cyclotron harmonic (ECH) waves, exohiss, magnetosonic (MS) waves, and electromagnetic ion cyclotron (EMIC) waves, based on the observations from Van Allen Probe A on October 15, 2015. The diffusion coefficients induced by these waves are calculated by using both the Full Diffusion Code and test particle simulations. Moreover, the scattering effects of these waves on energetic electrons are simulated by using a two-dimensional Fokker–Planck diffusion model. The results show that ECH waves mainly scatter low-pitch-angle (< 20°) electrons at 0.1–10 keV; exohiss can significantly scatter hundreds of kiloelectron volt electrons to form a reversed energy spectrum; MS waves mainly affect high-pitch-angle electrons (> 60°); and EMIC waves scatter only > 5 MeV electrons. The combined scattering effects of exohiss and MS waves are stronger than those of exohiss alone. The top-hat pitch angle distributions produced by exohiss are relaxed after adding the effect of MS waves. Because the energies of electrons scattered by ECH waves and EMIC waves are much lower and higher than those scattered by exohiss and MS waves, respectively, the combined scattering effects with the addition of ECH and EMIC waves show little difference from the results for the combination of MS waves and exohiss. These results suggest that distinct wave modes can occur simultaneously and scatter electrons in combination or individually, which requires careful consideration in future global simulations of the complex dynamics of radiation belt energetic electrons.

Keywords: ECH waves; exohiss; MS waves; EMIC waves; radiation belts

1. Introduction

The Earth's radiation belts, which are also called the Van Allen belts, consist of energetic electrons trapped by the geomagnetic field (e.g., Baker et al., 1986; Li XL et al., 1997), in which electrons undergo gyration, bounce, and drift motions. The energetic electron fluxes are affected by the combination of acceleration, transportation, and loss processes within the magnetosphere (Reeves et al., 2003; Ma X et al., 2020). Wave–particle interactions are important for radiation belt dynamics and can significantly change the pitch angle distributions (PADs) and energy spectrum of electrons (Li LY et al., 2005; Summers et al., 2007a, b; Thorne, 2010; Ni BB et al., 2015).

Several typical plasma wave modes observed in the outer radiation belt ($3 < L < 6$) are believed to contribute to scattering energetic electrons. Electrostatic electron cyclotron harmonic (ECH) waves are usually observed outside the plasmapause close to the magnetic equator, propagating almost perpendicularly to the ambient magnetic field in bands between the harmonics of the electron gyrofrequency (f_{ce}) with the dominant wave power centered around $(n + 1/2)f_{ce}$ (Kennel et al., 1970; Roeder and Koons, 1989; Meredith et al., 2009; Ni BB et al., 2017a, b; Lou YQ et al., 2018; Guo DY et al., 2021). Electron cyclotron harmonic waves can resonate with plasma sheet electrons at hundreds of electron volts to ~10 keV and scatter them into the loss cone, resulting in

Correspondence to: Z. Xiang, xiangzheng@whu.edu.cn
X. D. Gu, guxudong@whu.edu.cn
Received 31 AUG 2022; Accepted 25 OCT 2022.
Accepted article online 11 NOV 2022.

the generation of the nightside diffuse aurora (Lui et al., 1977; Meng et al., 1979; Ni BB et al., 2008, 2016; Frey et al., 2019; Zhang XJ et al., 2019). Electron cyclotron harmonic waves also contribute to the pulsating aurora at higher L values.

Plasmaspheric hiss is a kind of incoherent, broadband whistler mode emission generally confined within the dense plasma environment, such as the plasmasphere and plasmaspheric plumes, with a frequency range of ~100 Hz to a few kilohertz (Thorne et al., 1973; Chappell, 1974; Carpenter et al., 1993; Laakso et al., 2015; Yu J et al., 2017; Su ZP et al., 2018; Guo DY et al., 2021; Li HM et al., 2022; Yang L et al., 2022). However, hiss captured outside the plasmapause, which is called exohiss, can primarily be observed in the dayside high-latitude ($\lambda > 35°$) region (Russell et al., 1970; Thorne et al., 1973). Statistical results indicate that plasmaspheric hiss is a major source of exohiss waves outside the plasmapause (Wang JL et al., 2020). Plasmaspheric hiss is thought to be the major generating mechanism of the slot region that occurs between the inner and outer radiation belts by pitch-angle scattering of energetic electrons at a wide energy range from a few kiloelectron volts to >1 MeV (Lyons and Thorne, 1973; Meredith et al., 2006; Summers et al., 2008; Ni BB et al., 2013; Thorne et al., 2013; Zhu H et al., 2015; Xiang Z et al., 2020a; Xiang Z et al., 2020b), and can form a reversed energy spectrum (Ni BB et al., 2019).

Magnetosonic (MS) waves (also called equatorial noise) are highly oblique electromagnetic emissions frequently observed within 5° of the magnetic equator, both inside and outside the plasmasphere (Russell et al., 1970; Santolík et al., 2004; Němec et al., 2005, 2006; Li LY et al., 2017a; Liu B et al., 2018; Fan F et al., 2021). Magnetosonic waves are generated in the frequency range between the local proton gyrofrequency (f_{ce}) and the lower hybrid resonance frequency (f_{LHR}) by unstable proton ring distributions (Perraut et al., 1982; Laakso et al., 1990; Santolík et al., 2002; Horne et al., 2007; Chen LJ et al., 2010; Jordanova et al., 2012; Ma QL et al., 2014). Magnetosonic waves can scatter energetic electrons, resulting in the formation of butterfly distributions (Shprits et al., 2009; Ma QL et al., 2015, 2016; Li JX et al., 2016b; Li LY et al., 2017b; Li HM et al., 2020).

Electromagnetic ion cyclotron (EMIC) waves are observed with frequencies below the distinct ion gyrofrequency (f_{H^+}, f_{He^+}, and f_{O^+}). Rapid losses of radiation belt relativistic electrons and >100 keV ring current protons can be caused by cyclotron-resonant interactions with EMIC waves (Thorne and Kennel, 1971; Summers et al., 2004, 2007a, b; Liu KJ et al., 2012; Shprits et al., 2013; Usanova et al., 2014; Ni BB et al., 2015; Yu J et al., 2015; Li LY et al., 2016; Shprits, 2016; Xiang Z et al., 2018, 2021; Xue ZX et al., 2021; Cao X et al., 2020).

Although different wave modes have different excitation mechanisms, they are all associated with particle distributions and are more likely to be observed after active geomagnetic states, which makes this simultaneously observation of four wave modes possible. Electron cyclotron harmonic waves are thought to be generated by a loss-cone distribution (Ashour-Abdalla and Kennel, 1978; Horne et al., 1981). Plasmaspheric hiss can be excited by the anisotropic instability of hot electrons (Chen LJ et al., 2012; Tang RX and Summers, 2019). Exohiss is suggested to be a production of the leakage of plasmaspheric hiss (Thorne et al., 1979; Zhu H et al., 2015). Magnetosonic waves and EMIC waves are generated in the inner magnetosphere and mainly arise from the ring current protons near the equatorial plane (Kennel and Engelmann, 1966). Magnetosonic waves are driven by energetic protons at energies of tens of kiloelectron volts with a positive energy gradient (Curtis and Wu CS, 1979; Perraut et al., 1982; Chen LJ et al., 2010; Liu KJ et al., 2011; Xiao FL et al., 2013; Ma QL et al., 2014), and EMIC waves are attributed to the cyclotron resonance instability of thermally anisotropic ring current protons with energies in the range of ~1–100 keV (Cornwall, 1965; Kennel and Petschek, 1966; Gary et al., 1995; Chen LJ et al., 2009). Previous studies have demonstrated that electrons can be scattered by two wave modes simultaneously. Xiao FL et al. (2015) suggested that the combined acceleration by chorus and magnetosonic waves can explain the electron flux evolution in both the energy and butterfly PAD. Ni BB et al. (2017b) investigated the competitive effects on electron dynamics attributable to plasmaspheric hiss and MS waves. Teng SC et al. (2021) and Zhou RX et al. (2022) analyzed the cooperation between EMIC waves and MS waves upon electron loss at several megaelectron volts. The competitive influences of different plasma waves on radiation belt electrons depend on the density of ambient plasmas and the relative intensity of the waves (Li LY et al., 2017a, 2021, 2022; Yu J et al., 2020)

In this study, we report a representative case of four concurrent wave modes at $L \approx 5.0$, namely, ECH waves, exohiss, MS waves, and EMIC waves, observed by Van Allen Probe A on October 15, 2015. To quantify the scattering effects of simultaneously observed multimode waves on energetic electrons both separately and jointly, the diffusion coefficients of electrons induced by these waves are calculated and two-dimensional (2-D) Fokker–Planck diffusion simulations are performed. The satellite observations are shown in Section 2. Section 3 presents the results of the diffusion coefficient calculations and the 2-D Fokker–Planck diffusion simulations. Finally, the conclusions are summarized in Section 4.

2. Event Overview and Model Adoption

2.1 Instrumentation and Event Overview

The twin-satellite Van Allen Probes mission was launched into an equatorial elliptical orbit with a distance range from ~1.1 R_E (radius of the Earth) to ~6.5 R_E on August 30, 2012, providing high-quality data sets that included the ambient magnetic field, background plasma density, radiation belt particle fluxes, and electromagnetic field and waves (Mauk et al., 2013). In this study, the Electric and Magnetic Field Instrument Suite and Integrated Science (EMFISIS; Kletzing et al., 2013) is used to provide both electric and magnetic field data. The EMFISIS suite contains the high-frequency receiver (HFR) and the waveform frequency receiver (WFR), which can measure the wave properties in a wide frequency range from ~10 to ~500 kHz. The Level 4 data sets of the Van Allen Probes are applied to acquire the ambient plasma density information, which is extracted from the trace of the upper hybrid resonance frequency measured by the HFR (Kurth et al., 2015). Helium, Oxygen, Proton, and Electron (HOPE) instrument (Funsten et al., 2013) measurements are used to obtain the hot electron distribution.

Figure 1 shows a simultaneously occurring multimode wave event

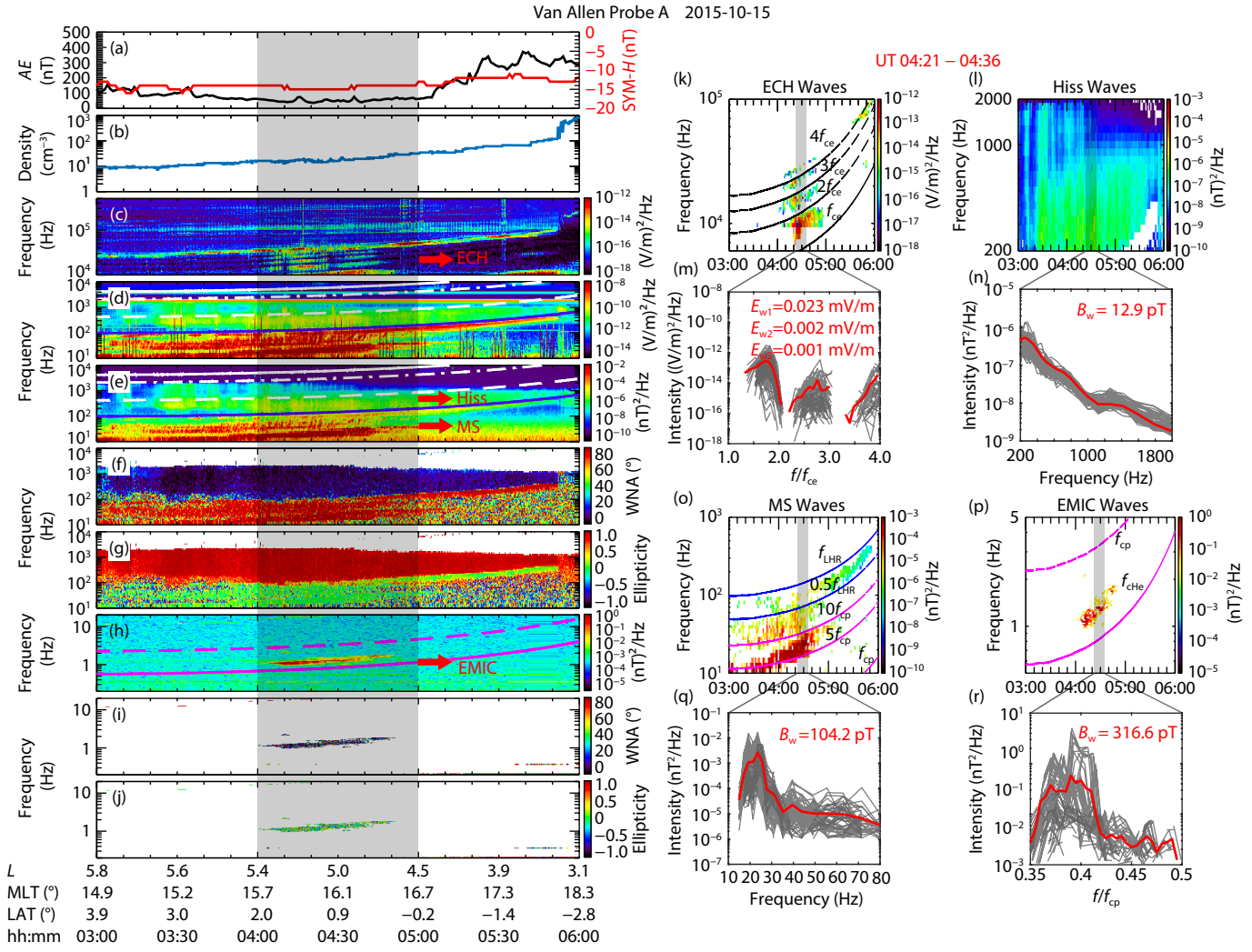

Figure 1. Plasma wave observations from Van Allen Probe A from 03:00 to 06:00 UT on October 15, 2015. (a) Auroral electrojet (*AE*) and SYM-*H* indices. (b) Background electron density. (c) Spectrograms of the electric field power spectral intensity measured by the high-frequency receiver (HFR). (d, e) Spectrograms of the electric and magnetic field power spectral intensity measured by the waveform frequency receiver (WFR). The white curves represent the equatorial electron gyrofrequency f_{ce} (solid), 0.5 f_{ce} (dotted and dashed), and 0.1 f_{ce} (dashed), and the blue curve indicates the lower hybrid resonance frequency f_{LHR} (solid), respectively. (f, g) Ellipticity and wave normal angle corresponding to the WFR measurements. (h) Power spectrum density derived from EMFISIS (Electric and Magnetic Field Instrument Suite and Integrated Science). The dashed line shows the local gyrofrequency of protons, whereas the solid line illustrates the local gyrofrequency of helium. (i, j) Wave ellipticity and wave normal angle of electromagnetic ion cyclotron (EMIC) waves. The gray-shaded bar (a–j) indicates the time period of the multimode wave event. (k, l, o, p) Filtered waves. (m, n, q, r) Wave spectral intensities. The gray curves show the wave spectral intensities, and the thick red curves represent the mean profiles of the power spectral densities derived from the shaded time period in (k), (l), (o), and (p) of 04:21–04:36 UT. ECH, electron cyclotron harmonic waves; Hiss, exohiss; MS, magnetosonic waves.

from 04:00 to 05:00 universal time (UT) on October 15, 2015. Four wave modes are observed in this event: ECH waves, exohiss, MS waves, and EMIC waves. Especially for the ECH waves and the EMIC waves, the two wave modes appear and disappear almost simultaneously despite their different excitation mechanisms. Figure 1a presents the auroral electrojet (*AE*) index (<300 nT during the selected time period) and the SYM-*H* index (less than −15 nT during the selected time period), indicating a relatively quiet geomagnetic environment. Meanwhile, both the small value of electron density in Figure 1b and the occurrence of the ECH waves in Figure 1c suggest that this event occurred outside the plasmapause. The exohiss waves observed by the WFR instrument in Figures 1d–1g are marked by a red arrow. The MS waves can be clearly observed, according to Figures 1d–1g, by the enhancement of the magnetic field power spectral density at frequencies below the lower hybrid resonance frequency (f_{LHR}, blue solid line in Figure 1e). Although parts of the MS waves overlap the exohiss, the two wave modes can be identified by the ellipticities and wave normal angles shown in Figures 1f and 1g. Figures 1h–1j display the H^+ band EMIC waves with frequencies between the proton gyrofrequency (f_{cp}, magenta dashed line in Figure 1h) and the helium gyrofrequency (f_{He^+}, magenta solid line in Figure 1h).

We pick up four waves modes (Figures 1k, 1i, 1o, 1p) as well as the corresponding mean profiles of wave spectral intensities from 04:

21 to 04:36 UT, as indicated by the shaded regions in Figures 1m, 1n, 1q, and 1r when $L = 5 \pm 0.1$ ($N_e = 16.8$ cm^{-3}, MLT = 16.1°, LAT = 1°, and $B_{eq} = 218$ nT). The ECH waves have a typical structure that the first band waves—between f_{ce} (electron resonance frequency) and 2 f_{ce}, having most of the energy according to the amplitudes—denoted in Figure 1m. Note that Figure 1k is derived from a combination of HFR and WFR instrument spectra because these two instruments both capture part of the ECH waves. The exohiss waves in Figure 1l occur at frequencies ranging from 200 to 2,000 Hz, and the amplitude is 12.9 pT, as marked in the upper right corner of Figure 1n. The amplitude of the MS waves shown in Figure 1o is 104.2 pT, as derived from Figure 1q. For the H^+ band EMIC waves, the averaged amplitude is 316.6 pT in the specific period, as shown in Figure 1r.

2.2 ECH Wave Model

To obtain the bounce-averaged diffusion coefficients induced by ECH waves, the information on wave propagation characteristics, such as the wave normal angle and the wave power spectrum, are required (Ni BB et al., 2011; Lou YQ et al., 2021). In this study, the WHAMP (waves in homogeneous, anisotropic, multicomponent plasmas) code (Rönnmark, 1982) is adopted to evaluate the scattering effects of the ECH waves. The WHAMP calculates the dispersion relationship of waves with the assumption of homogeneous, anisotropic, magnetized plasma. As the inputs of the WHAMP code, the phase space density (PSD) of energetic electrons is expressed by the sum of the subtracted Maxwellian distribution given by Ashour-Abdalla and Kennel (1978):

$$f_i\left(v_\perp, v_\parallel\right) = \frac{n_i}{\pi^{\frac{3}{2}} \alpha_{\perp i}^2 \alpha_{\parallel i}} \exp\left(-\frac{v_\parallel^2}{\alpha_{\parallel i}^2}\right) \left\{\Delta_i \exp\left(-\frac{v_\perp^2}{\alpha_{\perp i}^2}\right) + \frac{1-\Delta_i}{1-\beta_i}\left[\exp\left(-\frac{v_\perp^2}{\alpha_{\perp i}^2}\right) - \exp\left(-\frac{v_\perp^2}{\beta_i \alpha_{\perp i}^2}\right)\right]\right\}, \quad (1)$$

where the subscript i represents the ith component of energy electrons, f is the PSD of electrons, n is the electron density, $\alpha_\parallel$ and $\alpha_\perp$ denote the thermal velocities parallel and perpendicular to the ambient magnetic field, and Δ and β determine the depth and width of the loss cone, respectively.

To obtain the precise dispersion relation of ECH waves, the averaged electron PSD derived from the HOPE instrument from 04:21 to 04:36 UT with an energy range from ~25 eV to ~50 keV (the full 72 energy channels) is fitted by summing the nine components with the subtracted Maxwellian distribution. The PSDs shown in Figure 2 are induced from the flux data inferred by HOPE during the investigated time period. Figure 2a shows the observation (solid lines) and simulation (dashed lines) of the electron PSDs by taking the natural logarithm, whereas Figure 2b shows the PSDs as a function of the pitch angles. The parameters of the fitted electron components are shown in Table 1. Figures 1c–1e are normalized frequencies, wavenumbers, and growth rates as a function of the wave normal angles, respectively.

Figures 2a and 2b clearly show that our fitted results of the electron PSDs match the observations well. Loss-cone distributions, which are important for the excitation of ECH waves, can be clearly observed in Figure 2a. In Figure 2b, an isotropic distribution is shown below ~100 eV, and the pancake PADs can be recognized at higher energies. On the basis of the modeled electron distributions, we calculate the dispersion relation of seven specific frequencies, which are adopted from 1.3 f_{ce} to 1.9 f_{ce} with an increment of 0.1 f_{ce}; the results are demonstrated in Figures 2c–2e. The simulated growth rates of ECH waves shown in Figure 2e have a peak at 1.6 $\frac{f}{f_{ce}}$, which matches the satellite observation well. In addition, the maximum growth rate for 1.5–1.7 $\frac{f}{f_{ce}}$ is likely to arise at the wave normal angles around 88.5°, whereas it is > 89° for wave frequencies at 1.3, 1.4, 1.8, and 1.9 $\frac{f}{f_{ce}}$. Consequently, the farther away from the central frequency of 1.6 $\frac{f}{f_{ce}}$, the larger is the wave normal angle corresponding to the peak growth rate for a certain frequency.

3. Simulation Results

3.1 Wave-Induced Electron Scattering Rates

To quantify the combined scattering effects on electrons by the four wave modes, the bounce-averaged electron diffusion coefficients induced by each wave mode are evaluated individually. The Full Diffusion Code (FDC) is adopted to compute the quasilinear bounce-averaged electron diffusion coefficients by exohiss, EMIC waves, and ECH waves. Their resonance harmonics $|N| \leq 10$ are considered (Ni BB et al., 2008, 2022; Liu YXZ et al., 2022). Because of the different propagation characteristics of these three wave modes, we adopt different latitude ranges for exohiss ($|\mathrm{LAT}| \leq 40°$), EMIC waves ($|\mathrm{LAT}| \leq 40°$), and ECH waves ($|\mathrm{LAT}| \leq 3°$). Exohiss takes a wave normal angle model following Ni BB et al. (2013), EMIC waves adopt the wave normal angle model introduced in Ni BB et al. (2015) and assume the ionic components of η_{H^+}= 85%, η_{He^+} = 10%, η_{O^+} = 5% in the same energy range. For ECH waves, we focus on the first harmonic band because the wave power of the first harmonic band dominates over the other harmonic bands in the selected ECH wave event. We adopt the wave frequency spectrum from the observation frequencies (~1.3–1.9 f_{ce}) with an increment of 0.1 f_{ce}. In particular, the scattering effect of ECH waves simulated by the FDC is conducted on the energy range from 10 eV to 100 keV because of the wave–particle resonance energy range. For MS waves, we adopt the test particle code to simulate the electron scattering effect of Landau resonances and transit-time diffusion with $|\mathrm{LAT}| \leq 3°$ and pitch angle $\theta = 89°$ following previous studies (Horne et al., 2007; Ni BB et al., 2017a, 2018). The main parameters required are summarized in Table 2.

Figure 3 displays the 2-D bounce-averaged pitch angle, cross diffusion (pitch angle, momentum), and momentum diffusion coefficients at $L = 5$ (corresponding to the gray shaded region in Figure 1). For exohiss, the pitch angle diffusion rates in Figure 3a show an effective diffusion on hundreds of kiloelectron volt electrons with a time scale of approximately one day. Two regions show strong diffusion rates. The part near the high pitch angle is due to Landau resonance, whereas the region corresponding to a wider pitch angle range results from the cyclotron resonances. The coefficients of cross diffusion and momentum diffusion by exohiss are also considerable, with maximum diffusion rates of ~10^{-5} s^{-1} for electrons at ~100 keV with pitch angles ranging from

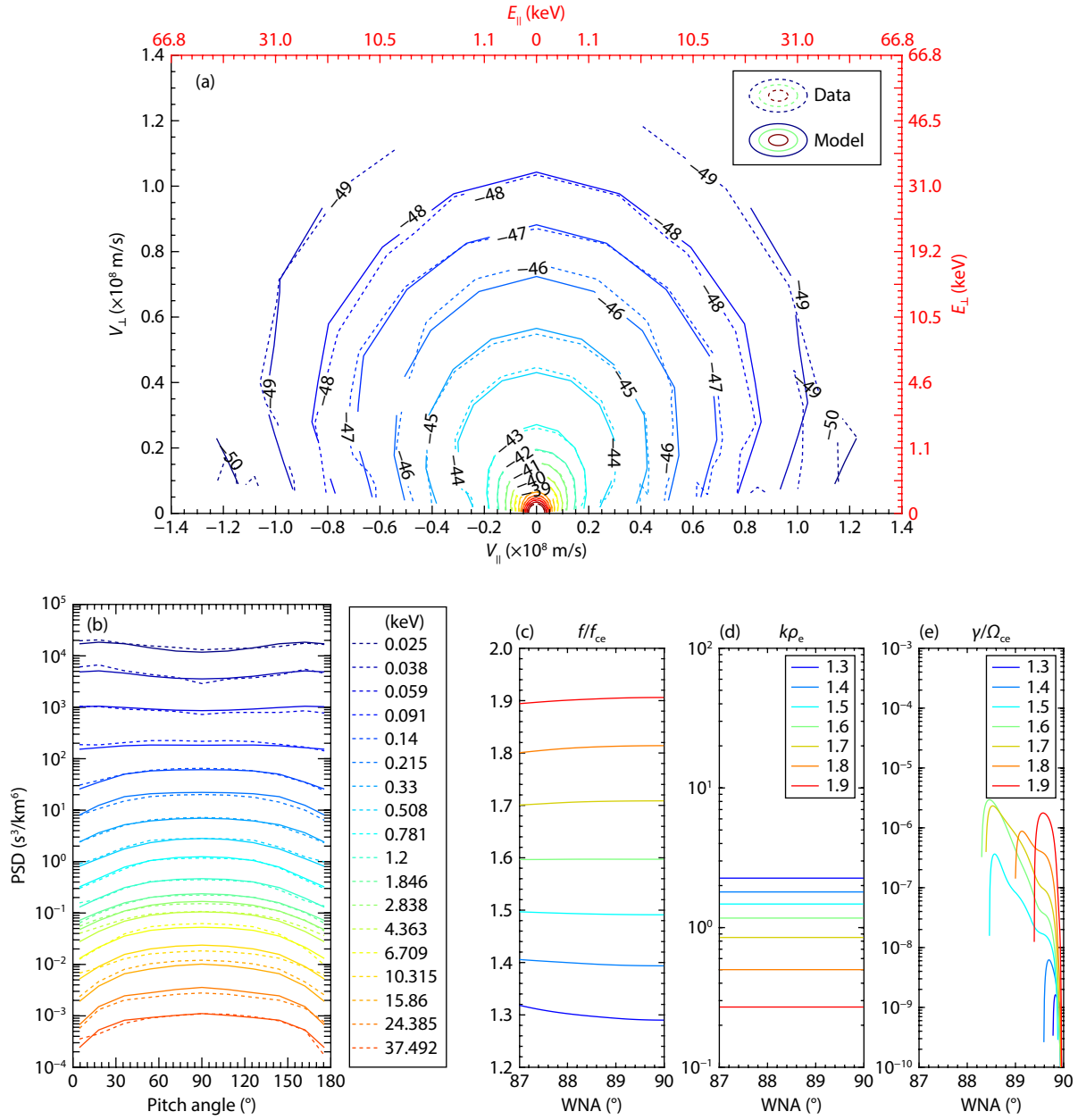

Figure 2. (a) Contours of the electron phase space density (PSD) in electron velocity ($v_{||}$, $v_\perp$) space (or in kinetic energy ($E_{||}$, $E_\perp$) space, marked by the red axis) from 04:21 to 04:36 UT. The dashed curves illustrate the observational electron PSD obtained from the HOPE (Helium, Oxygen, Proton, and Electron) instrument, and the solid curves denote the distribution of energetic electrons modeled by the sum of the subtracted Maxwellian components. (b) Observed and fitted averaged electron PSD as a function of the pitch angle. (c) Simulated frequencies normalized to f_{ce} from 1.3 to 1.9 as a function of the wave normal angle (WNA). (d) Wavenumber k normalized to the gyroradius ρ_e of 1 eV component. (e) The corresponding normalized growth rates $\frac{\gamma}{\Omega_{ce}}$ of the wave frequency at 1.3–1.9 $\frac{f}{f_{ce}}$.

40° to ~90°. The diffusion coefficients of MS waves are mainly in the range of 100 keV–1 MeV, with pitch angles ranging from 50° to 80° in Figures 3d–3f (Bortnik and Thorne, 2010; Fu S et al., 2019). The momentum scattering rates are comparable to the pitch angle diffusion rates for MS waves, suggesting a feasible acceleration mechanism. According to the quasilinear theory, the amplitudes of waves have a quadratic effect on the calculation result of the diffusion coefficient. Although the amplitude of MS waves in this case is several times greater than that of exohiss, to show the transit-time diffusion, we adapt the test particle simulations instead of the FDC, whose combined scattering rates are generally an order of magnitude weaker because the electrons are moved out of the Landau resonance by the advective effect of the bounce resonance (Fu S et al., 2019). In contrast, EMIC waves show a significant diffusion effect on electrons above 5 MeV with a time scale of minutes, which is more remarkable than that of exohiss because of the much larger amplitude. Regarding the combined scattering effect of concurrent exohiss and MS waves, Hua M et al. (2019) suggested that when exohiss is comparable to or stronger than MS waves, the combined scattering effect is mainly featured

Table 1. The nine electron components used to fit the measured electron phase space density from 04:21 to 04:36 UT.

Component	N_e (m^{-3})	$T_{\|\|}$ (eV)	$T_\perp$ (eV)	Δ	β
1	1.2×10^7	1.0	1.0	1.0	0.5
2	4.5×10^6	12.2	13.7	1.0	0.0
3	2.2×10^5	64.0	64.0	0.4	0.4
4	5.3×10^4	256.0	256.0	0.4	0.7
5	4.0×10^4	1,648.6	2,057.0	0.3	0.7
6	3.1×10^4	5,215.0	5,162.3	0.1	0.7
7	5.4×10^3	3,200.0	6,100.0	0.5	0.0
8	4.2×10^3	15,350.1	28,450.0	0.0	0.2
9	1.3×10^4	77,102.7	25,600.0	0.6	0.4

Table 2. Parameters required for calculating the diffusion coefficients.[a]

Parameter	Wave mode			
	ECH	Exohiss	MS	EMIC
Amplitude	0.023 mV/m	12.9 pT	104.2 pT	316.6 pT
LAT	≤ 3°	≤ 40°	≤ 3°	≤ 40°
$\|N\|$	≤ 10	≤ 10	0	≤ 10
WNA	Table 1	following Ni et al. (2013)	89°	following Ni et al. (2015)
Other	L = 5, N_e = 16.8 cm^{-3}, B_{eq} = 218 nT			

[a]ECH, electron cyclotron harmonic waves; MS, magnetosonic waves; EMIC, electromagnetic ion cyclotron waves; LAT, latitude; N, resonance harmonics; WNA, wave normal angle.

by exohiss—induced pitch angle scattering, which can produce butterfly PADs for less than ~1 MeV electrons by strong exohiss, top—hat PADs for less than ~150 keV electrons, and flat—top PADs for greater than ~300 keV electrons by both weak and strong exohiss. Pitch angle diffusion by intense exohiss can also drive a considerable PSD valley between ~50 keV and 1 MeV. Because of the small amplitude, ECH waves have only weak effects on electrons from tens of electron volts to tens of kiloelectron volts at small pitch angles (< 20°). According to the diffusion energy range of the four wave modes, exohiss and MS waves are likely to have a combined scattering effect on electrons at hundreds of kiloelectron volts, but this is far away from the main energy range of strong diffusion coefficients induced by EMIC waves and ECH waves.

3.2 Evaluation of the PSD Evolution of Energetic Electrons

With the acquisition of individual bounce-averaged diffusion rates induced by ECH waves, exohiss, MS waves, and EMIC waves, we perform a 2-day wave-induced evolution simulation of the energetic electron PSD by numerically solving the 2-D Fokker–Planck equation:

$$\frac{\partial f}{\partial t}=\frac{p^2}{G}\frac{\partial}{\partial \alpha_{eq}}\left(\left\langle D_{\alpha_{eq}\alpha_{eq}}\right\rangle\frac{G}{p^2}\frac{\partial f}{\partial \alpha_{eq}}+\left\langle D_{\alpha_{eq}p}\right\rangle\frac{G}{p^2}\frac{\partial f}{\partial p}\right)+\frac{1}{p}\frac{\partial}{\partial p}\left(\left\langle D_{p\alpha_{eq}}\right\rangle p^2\frac{\partial f}{\partial \alpha_{eq}}+\left\langle D_{pp}\right\rangle p\frac{\partial f}{\partial p}\right), \quad (2)$$

where α_{eq} is the equatorial pitch angle, $S(\alpha_{eq})$ denotes the normalized bounce time, where $S(\alpha_{eq})\approx 1.38-0.32\left[\sin\alpha_{eq}+(\sin\alpha_{eq})^{\frac{1}{2}}\right]$, and $G=p^2S(\alpha_{eq})\sin\alpha_{eq}\cos\alpha_{eq}$. In addition, f is the electron PSD, which is related to electron flux j and electron momentum p by $f=\frac{j}{p^2}$. And $\left\langle D_{\alpha_{eq}\alpha_{eq}}\right\rangle$, $\left\langle D_{pp}\right\rangle$, and $\left\langle D_{\alpha_{eq}p}\right\rangle=\left\langle D_{p\alpha_{eq}}\right\rangle$ demonstrate the bounce-averaged diffusion coefficients in pitch angle, momentum, and cross pitch angle momentum (Summers et al., 2007a; Xiao FL et al., 2009). We compute the electron PSDs at all pitch angles with the initial condition derived from satellite observations. For the boundary condition in the energy space, we assume that the electron PSDs are constant at E_k = 1 keV and 10 MeV with f = 0 at 10 MeV (Summers et al., 2004; Li JX et al., 2016a). For the boundary condition in the equatorial pitch angle space, we take f = 0 inside the loss cone and $\frac{\partial f}{\partial \alpha_{eq}}=0$ at $\alpha_{eq}=90°$.

Figure 4 presents the simulated temporal evolution of radiation belt electron PSDs at L = 5 under the influence of (a–e) exohiss, (f–j) MS waves, (k–o) exohiss combined with MS waves, (p–t) the combination of exohiss, MS waves, and EMIC waves, and (u–y) ECH waves. The five columns indicate wave–particle interaction time stamps of 2 days, with an increment of 12 hours. As illustrated in Figure 4, (1) exohiss can cause electron PSD decay at a wide energy range below megaelectron volts, especially around 100 keV electrons, resulting in the formation of a reversed energy spectrum, as shown in Figures 4d–4e; (2) the scattering effect of MS waves is most efficient in hundreds of kiloelectron volts, which

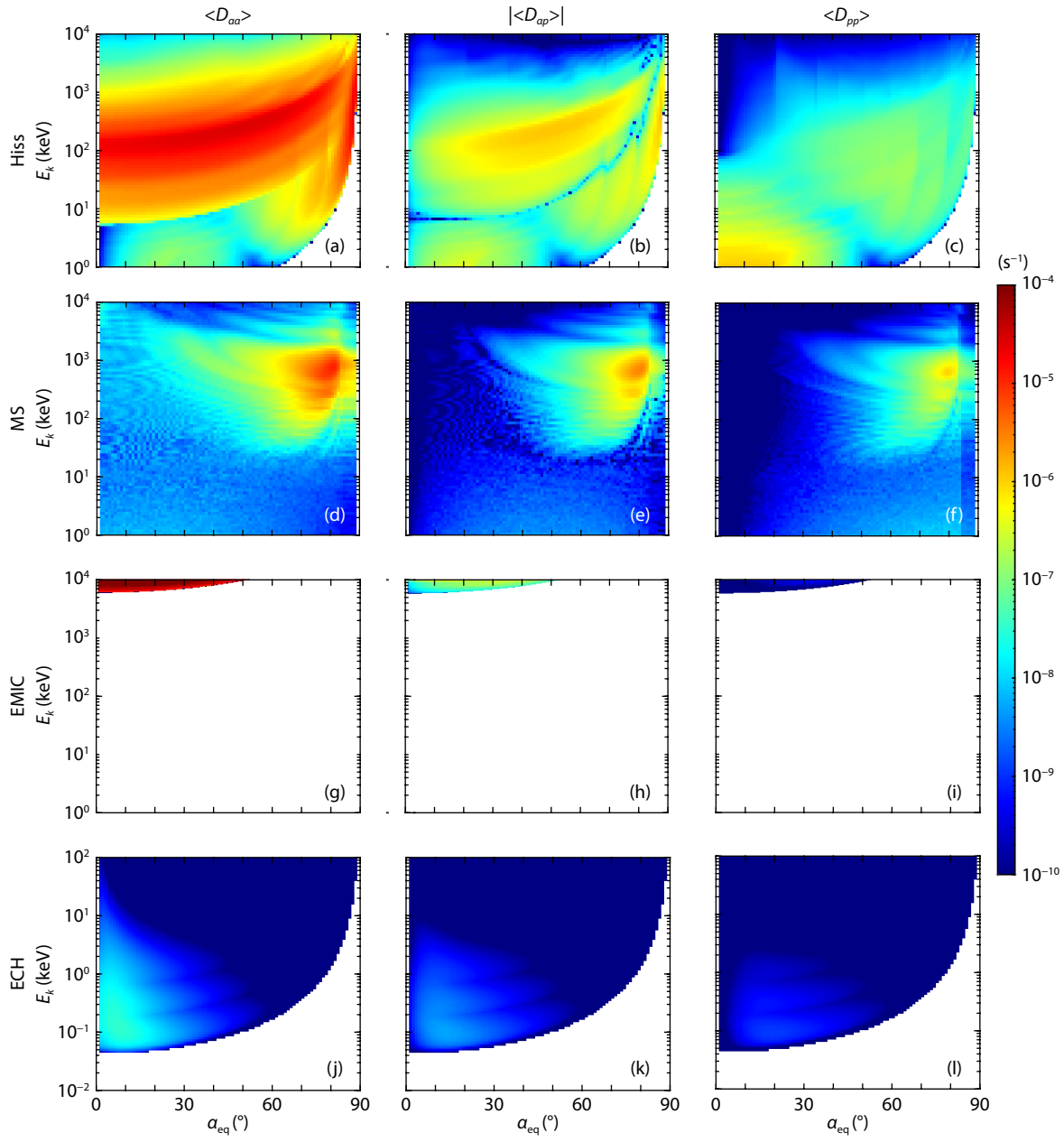

Figure 3. Two-dimensional plots of the bounce-averaged pitch angle, cross, and momentum diffusion coefficients (from left to right: <D_{aa}>, |<D_{ap}>|, <D_{pp}>) as a function of the equatorial pitch angles and electron kinetic energies E_k at L = 5 induced by (a–c) exohiss, (d–f) magnetosonic (MS) waves, (g–i) electromagnetic ion cyclotron (EMIC) waves, and (j–l) electron cyclotron harmonic (ECH) waves.

can scatter particles at pitch angles above 60°, forming butterfly distributions; (3) compared with exohiss scattering alone, the overall PSD decay from the combination of exohiss and MS waves is enhanced, but the butterfly distributions caused by MS waves are inhibited by exohiss; (4) when EMIC waves are included in the diffusion coefficients because of the combination of exohiss and MS waves, no clear difference occurs because of the high resonance energy of EMIC waves (> 5 MeV); (5) ECH waves can scatter < 20° electrons at a 0.1–10 keV energy range into loss cones effectively.

To display the contributions by the different wave modes on the PSD evolution more clearly, Figure 5 shows the temporal evolution of the simulated electron PSDs at the color-coded electron energies within 48 h under the impact of exohiss and MS waves individually and in combination. As shown in Figures 5a–5e, the scattering effects of electrons by exohiss on 100 keV are significantly stronger than those of other energies, causing the PSD to decrease by more than one order of magnitude in 2 days for electrons at pitch angles less than ~88°, forming top-hat PADs. Magnetosonic waves alone can scatter $\alpha_{eq} > 60°$ hundreds of kilo-electron volt electrons within 1 day, leading to the butterfly distributions in Figures 5f–5j. We found that the top-hat distribution induced by exohiss and the butterfly distribution induced by MS waves are both mainly caused by their cross-diffusion coefficients but that the former is positive and the latter is negative. Thus, when considering the combination of those two cross-diffusion coefficients, we can see that the butterfly distributions caused by MS waves are substantially inhibited by exohiss and that the top-

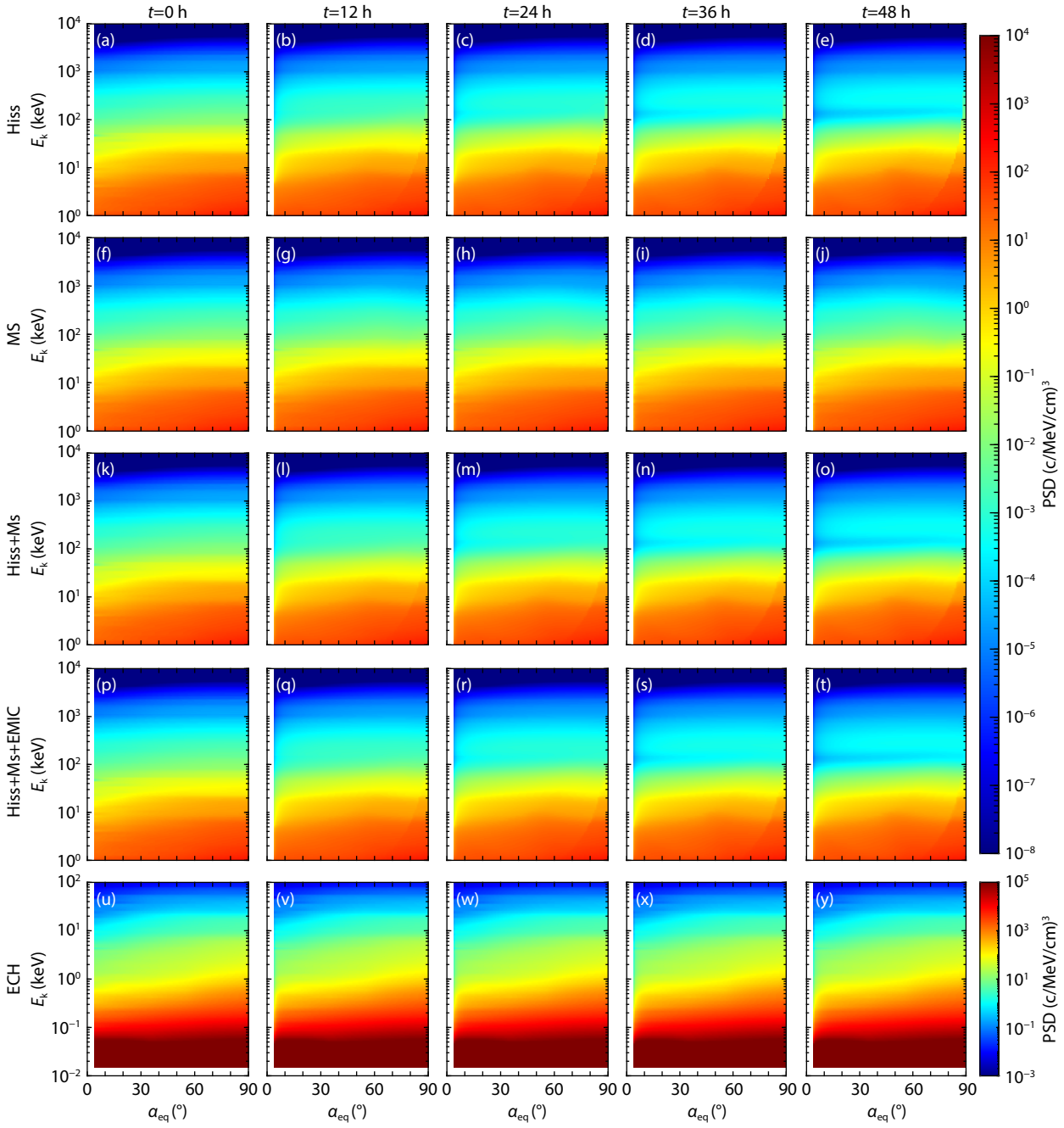

Figure 4. Two-dimensional temporal evolution of electron phase space density (PSD) under the impact of (a–e) exohiss, (f–j) magnetosonic (MS) waves, (k–o) a combination of exohiss and MS waves, (p–t) a combination of exohiss, MS waves, and electromagnetic ion cyclotron (EMIC) waves, and (u–y) electron cyclotron harmonic (ECH) waves in a time span of 2 days.

hat distributions caused by exohiss are inhibited by MS waves (Figures 5k–5o).

Because of the distinct resonant regions between EMIC waves (> 5 MeV), ECH waves (< 100 keV), exohiss, and MS waves (~100 keV–1 MeV), we display the PSD evolution caused by ECH waves and EMIC waves individually in Figure 6. In Figures 6a–6e, because of the rapid scattering in the order of minutes caused by EMIC waves on energetic electrons > 5 MeV with a pitch angle < 50°, electron PSDs reduce by 3 orders of magnitude within 12 hours and by 4 orders of magnitude within 48 hours, causing top-hat PADs. As shown in Figures 6f–6j, ECH waves can scatter ~100 eV to ~10 keV electrons with pitch angles <20° into loss cones.

4. Conclusions

In this study, we have reported a specific case of four concurrent magnetospheric wave modes, namely ECH waves, exohiss, MS waves, and EMIC waves, that were observed at $L \approx 5.0$ by Van Allen Probe A on October 15, 2015. The wave-induced quasilinear diffusion coefficients are calculated on the basis of the FDC and test particle simulations. By simulating the net electron diffusion process in terms of the 2-D Fokker–Planck diffusion simulations, we have investigated in detail the combined electron scattering

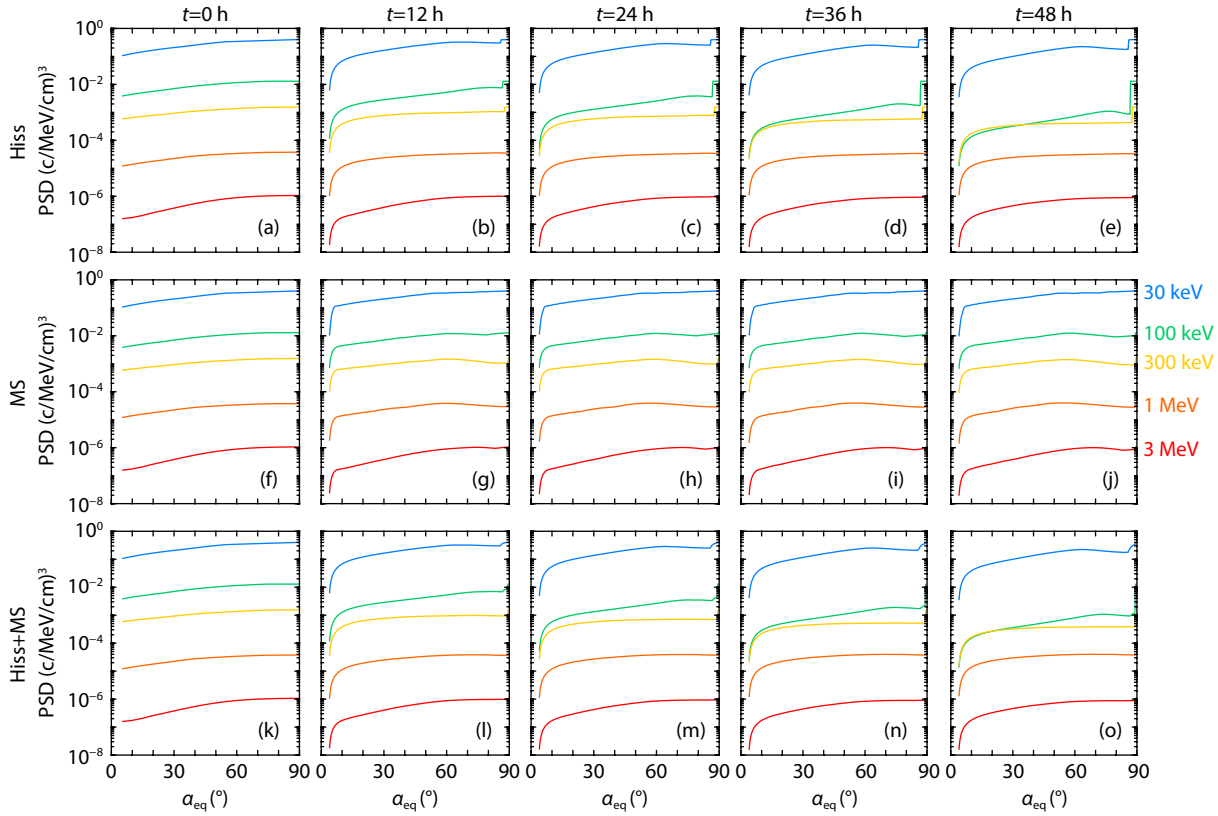

Figure 5. The simulated evolution of electron pitch angle distributions at selected energies over 2 days. (a–e) Exohiss (Hiss) waves, (f–j) magnetosonic (MS) waves, (k–o) a combination of exohiss and MS waves. PSD, phase space density.

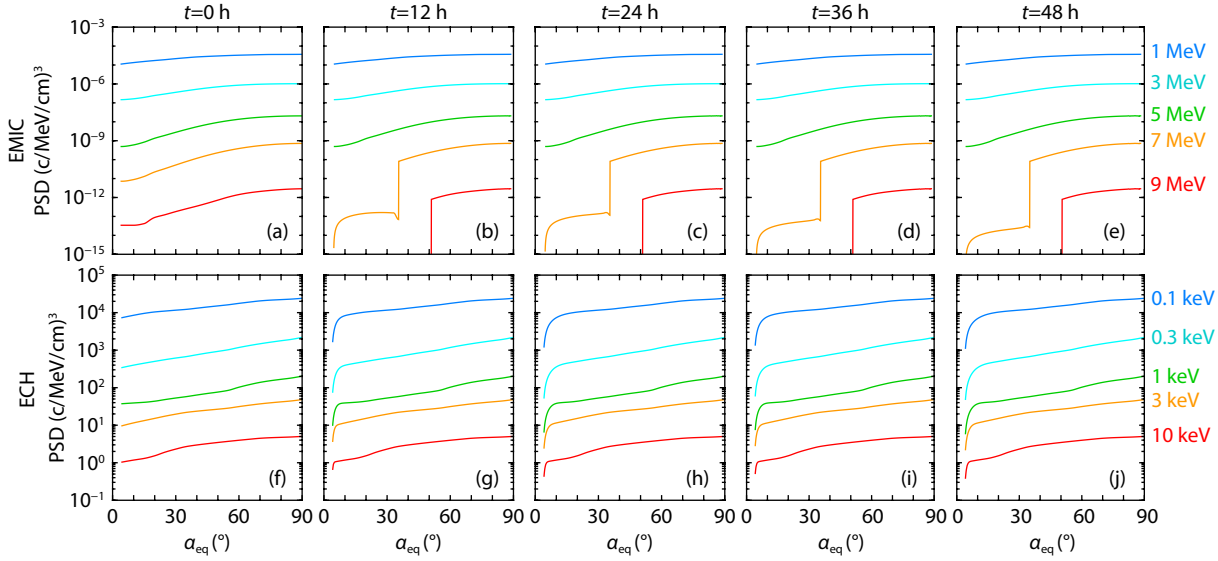

Figure 6. The simulated evolution of electron pitch angle distributions at selected energies over 2 days. (a–e) Electromagnetic ion cyclotron (EMIC) waves, and (f–j) electron cyclotron harmonic (ECH) waves.

effects of the four wave modes, in association with their competition and cooperation, upon the temporal evolution of the radiation belt electron distribution.

The main conclusions are summarized as follows:

(1) A representative case of simultaneously observed ECH waves, exohiss, MS waves, and EMIC waves at $L \approx 5.0$ is reported from 04:00 to 05:00 UT on October 15, 2015. The ECH waves and EMIC wave appeared and disappeared almost simultaneously despite their different excitation mechanisms.

(2) In this case, the scattering effects induced by the four wave modes are distinct: ECH waves mainly scatter low-pitch-angle (< 20°) electrons at 0.1–10 keV; exohiss can significantly scatter hundreds of kiloelectron volt electrons to form a reversed energy

spectrum; MS waves mainly affect high-pitch-angle electrons (> 60°); and EMIC waves scatter only > 5 MeV electrons.

(3) Regarding the combined scattering effect, the butterfly distributions caused by MS waves are substantially inhibited by exohiss, and the top-hat distributions caused by exohiss are inhibited by MS waves. Electron cyclotron harmonic waves and EMIC waves have a slight combined scattering effect with other waves.

Acknowledgments

This work was supported by the National Natural Science Foundation of China (Grant Nos. 42188101, 42174190, 42025404, and 41904143), the Fundamental Research Funds for the Central Universities (Grant No. 2042021kf0016), the B-type Strategic Priority Program of the Chinese Academy of Sciences (Grant No. XDB41000000), the pre-research projects on Civil Aerospace Technologies funded by the China National Space Administration (Grant Nos. D020308 and D020104), and the China Postdoctoral Science Foundation Project (Grant No. 2019M662700). We also thank the EMFISIS, MagEIS (Magnetic Electron Ion Spectrometer), REPT (Relativistic Electron Proton Telescope), and HOPE Science Teams of the Van Allen Probes for providing all the data sets used for this study. The EMFISIS data were obtained from https://emfisis.physics.uiowa.edu/data/index, the HOPE data were obtained from https://spdf.gsfc.nasa.gov/pub/data/, and the geomagnetic activity indices were obtained from the NASA OMNIWeb (http://cdaweb.gsfc.nasa.gov).

References

Ashour-Abdalla, M., and Kennel, C. F. (1978). Nonconvective and convective electron cyclotron harmonic instabilities. *J. Geophys. Res.: Space Phys.*, *83*(A4), 1531–1543. https://doi.org/10.1029/JA083iA04p01531

Baker, D. N., Blake, J. B., Klebesadel, R. W., and Higbie, P. R. (1986). Highly relativistic electrons in the Earth's outer magnetosphere: 1. Lifetimes and temporal history 1979–1984. *J. Geophys. Res.: Space Phys.*, *91*(A4), 4265–4276. https://doi.org/10.1029/ja091ia04p04265

Bortnik, J., and Thorne, R. M. (2010). Transit time scattering of energetic electrons due to equatorially confined magnetosonic waves. *J. Geophys. Res.: Space Phys.*, *115*(A7), A07213. https://doi.org/10.1029/2010ja015283

Cao, X., Ni, B. B., Summers, D., Shprits, Y. Y., and Lou, Y. Q. (2020). Effects of polarization reversal on the pitch angle scattering of radiation belt electrons and ring current protons by EMIC waves. *Geophys. Res. Lett.*, *47*(17), e2020GL089718. https://doi.org/10.1029/2020GL089718

Carpenter, D. L., Giles, B. L., Chappell, C. R., Décréau, P. M. E., Anderson, R. R., Persoon, A. M., Smith, A. J., Corcuff, Y., and Canu, P. (1993). Plasmasphere dynamics in the duskside bulge region: a new look at an old topic. *J. Geophys. Res.: Space Phys.*, *98*(A11), 19243–19271. https://doi.org/10.1029/93JA00922

Chappell, C. R. (1974). Detached plasma regions in the magnetosphere. *J. Geophys. Res.*, *79*(13), 1861–1870. https://doi.org/10.1029/ja079i013p01861

Chen, L. J., Thorne, R. M., and Horne, R. B. (2009). Simulation of EMIC wave excitation in a model magnetosphere including structured high-density plumes. *J. Geophys. Res.: Space Phys.*, *114*, A07221. https://doi.org/10.1029/2009JA014204

Chen, L. J., Thorne, R. M., Jordanova, V. K., and Horne, R. B. (2010). Global simulation of magnetosonic wave instability in the storm time magnetosphere. *J. Geophys. Res.: Space Phys.*, *115*(A11), A11222. https://doi.org/10.1029/2010JA015707

Chen, L. J., Li, W., Bortnik, J., and Thorne, R. M. (2012). Amplification of whistler-mode hiss inside the plasmasphere. *Geophys. Res. Lett.*, *39*(8), L08111. https://doi.org/10.1029/2012GL051488

Cornwall, J. M. (1965). Cyclotron instabilities and electromagnetic emission in the ultra low frequency and very low frequency ranges. *J. Geophys. Res.*, *70*(1), 61–69. https://doi.org/10.1029/JZ070i001p00061

Curtis, S. A., and Wu, C. S. (1979). Gyroharmonic emissions induced by energetic ions in the equatorial plasmasphere. *J. Geophys. Res.: Space Phys.*, *84*(A6), 2597–2607. https://doi.org/10.1029/JA084iA06p02597

Fan, K., Gao, X. L., Lu, Q. M., and Wang, S. (2021). Study on electron stochastic motions in the magnetosonic wave field: Test particle simulations. *Earth Planet. Phys.*, *5*(6), 592–600. https://doi.org/10.26464/epp2021052

Frey, H. U., Han, D. S., Kataoka, R., Lessard, M. R., Milan, S. E., Nishimura, Y., Strangeway, R. J., and Zou, Y. (2019). Dayside aurora. *Space Sci. Rev.*, *215*(8), 51. https://doi.org/10.1007/s11214-019-0617-7

Fu, S., Ni, B. B., Zhou, R. X., Cao, X., and Gu, X. D. (2019). Combined scattering of radiation belt electrons caused by Landau and bounce resonant interactions with magnetosonic waves. *Geophys. Res. Lett.*, *46*(17–18), 10313–10321. https://doi.org/10.1029/2019GL084438

Funsten, H. O., Skoug, R. M., Guthrie, A. A., MacDonald, E. A., Baldonado, J. R., Harper, R. W., Henderson, K. C., Kihara, K. H., Lake, J. E., … Chen, J. (2013). Helium, Oxygen, Proton, and Electron (HOPE) mass spectrometer for the radiation belt storm probes mission. *Space Sci. Rev.*, *179*(1–4), 423–484. https://doi.org/10.1007/s11214-013-9968-7

Gary, S. P., Thomsen, M. F., Yin, L., and Winske, D. (1995). Electromagnetic proton cyclotron instability: Interactions with magnetospheric protons. *J. Geophys. Res.: Space Phys.*, *100*(A11), 21961–21972. https://doi.org/10.1029/95JA01403

Guo, D. Y., Fu, S., Xiang, Z., Ni, B. B., Guo, Y. J., Feng, M. H., Guo, J. G., Hu, Z. J., Gu, X. D., …. Wang, Q. (2021). Prediction of dynamic plasmapause location using a neural network. *Space Wea.*, *19*(5), e2020SW002622. https://doi.org/10.1029/2020SW002622

Horne, R. B., Christiansen, P. J., Gough, M. P., Rönnmark, K. G., Johnson, J. F. E., Sojka, J., and Wrenn, G. L. (1981). Amplitude variations of electron cyclotron harmonic waves. *Nature*, *294*(5839), 338–340. https://doi.org/10.1038/294338a0

Horne, R. B., Thorne, R. M., Glauert, S. A., Meredith, N. P., Pokhotelov, D., and Santolík, O. (2007). Electron acceleration in the Van Allen radiation belts by fast magnetosonic waves. *Geophys. Res. Lett.*, *34*(17), L17107. https://doi.org/10.1029/2007GL030267

Hua, M., Ni, B. B., Li, W., Gu, X. D., Fu, S., Shi, R., Xiang, Z., Cao, X., Zhang, W. X., and Guo, Y. J. (2019). Evolution of radiation belt electron pitch angle distribution due to combined scattering by plasmaspheric hiss and magnetosonic waves. *Geophys. Res. Lett.*, *46*(6), 3033–3042. https://doi.org/10.1029/2018GL081828

Jordanova, V. K., Welling, D. T., Zaharia, S. G., Chen, L., and Thorne, R. M. (2012). Modeling ring current ion and electron dynamics and plasma instabilities during a high-speed stream driven storm. *J. Geophys. Res.: Space Phys.*, *117*(A9), A00L08. https://doi.org/10.1029/2011JA017433

Kennel, C. F., and Engelmann, F. (1966). Velocity space diffusion from weak plasma turbulence in a magnetic field. *Phys. Fluids*, *9*(12), 2377. https://doi.org/10.1063/1.1761629

Kennel, C. F., and Petschek, H. E. (1966). Limit on stably trapped particle fluxes. *J. Geophys. Res.*, *71*(1), 1–28. https://doi.org/10.1029/JZ071i001p00001

Kennel, C. F., Scarf, F. L., Fredricks, R. W., McGehee, J. H., and Coroniti, F. V. (1970). VLF electric field observations in the magnetosphere. *J. Geophys. Res.*, *75*(31), 6136–6152. https://doi.org/10.1029/JA075i031p06136

Kletzing, C. A., Kurth, W. S., Acuna, M., MacDowall, R. J., Torbert, R. B., Averkamp, T., Bodet, D., Bounds, S. R., Chutter, M., … Tyler, J. (2013). The Electric and Magnetic Field Instrument Suite and Integrated Science (EMFISIS) on RBSP. *Space Sci. Rev.*, *179*(1–4), 127–181. https://doi.org/10.1007/s11214-013-9993-6

Kurth, W. S., De Pascuale, S., Faden, J. B., Kletzing, C. A., Hospodarsky, G. B., Thaller, S., and Wygant, J. R. (2015). Electron densities inferred from plasma wave spectra obtained by the Waves instrument on Van Allen Probes. *J. Geophys. Res.: Space Phys.*, *120*(2), 904–914. https://doi.org/10.1002/2014JA020857

Laakso, H., Junginger, H., Roux, A., Schmidt, R., and de Villedary, C. (1990).

Magnetosonic waves above $f_c(H^+)$ at geostationary orbit: GEOS 2 results. *J. Geophys. Res.: Space Phys.*, *95*(A7), 10609–10621. https://doi.org/10.1029/JA095iA07p10609

Laakso, H., Santolik, O., Horne, R., Kolmasová, I., Escoubet, P., Masson, A., and Taylor, M. (2015). Identifying the source region of plasmaspheric hiss. *Geophys. Res. Lett.*, *42*(9), 3141–3149. https://doi.org/10.1002/2015GL063755

Li, H. M., Peng, Q. S., Tang, R. X., Zhang, H., Zhong, Z. H., Deng, X. H., and Wang, D. D. (2020). Statistical characteristics of electron pitch angle distributions inside the magnetopause based on MMS observations. *J. Geophys. Res.: Space Phys.*, *125*(10), e2020JA028291. https://doi.org/10.1029/2020JA028291

Li, H. M., Fu, T. X., Tang, R. X., Yuan, Z. G., Yang, Z. R., Ouyang, Z. H., and Deng, X. H. (2022). Statistical study and corresponding evolution of plasmaspheric plumes under different levels of geomagnetic storms. *Ann. Geophys.*, *40*(2), 167–177. https://doi.org/10.5194/angeo-40-167-2022

Li, J. X., Bortnik, J., Thorne, R. M., Li, W., Ma, Q. L., Baker, D. N., Reeves, G. D., Fennell, J. F., Spence, H. E., … Blake, J. B. (2016a). Ultrarelativistic electron butterfly distributions created by parallel acceleration due to magnetosonic waves. *J. Geophys. Res.: Space Phys.*, *121*(4), 3212–3222. https://doi.org/10.1002/2016JA022370

Li, J. X., Ni, B. B., Ma, Q. L., Xie, L., Pu, Z. Y., Fu, S. Y., Thorne, R. M., Bortnik, J., Chen, L. J., … Summers, D. (2016b). Formation of energetic electron butterfly distributions by magnetosonic waves via Landau resonance. *Geophys. Res. Lett.*, *43*(7), 3009–3016. https://doi.org/10.1002/2016GL067853

Li, L. Y., Cao, J. B., and Zhou, G. C. (2005). Combined acceleration of electrons by whistler-mode and compressional ULF turbulences near the geosynchronous orbit. *J. Geophys. Res.: Space Phys.*, *110*, A03203. https://doi.org/10.1029/2004JA010628

Li, L. Y., Yu, J., Cao, J. B., and Yuan, Z. G. (2016). Compression-amplified EMIC waves and their effects on relativistic electrons. *Phys. Plasmas*, *23*(6), 062116. https://doi.org/10.1063/1.4953899

Li, L. Y., Liu, B., Yu, J., and Cao, J. B. (2017a). The rapid responses of magnetosonic waves to the compression and expansion of Earth's magnetosphere. *Geophys. Res. Lett.*, *44*(22), 11239–11247. https://doi.org/10.1002/2017GL075649

Li, L. Y., Yu, J., Cao, J. B., Yang, J. Y., Li, X., Baker, D. N., Reeves, G. D., and Spence, H. (2017b). Roles of whistler mode waves and magnetosonic waves in changing the outer radiation belt and the slot region. *J. Geophys. Res.: Space Phys.*, *122*(5), 5431–5448. https://doi.org/10.1002/2016JA023634

Li, L. Y., Wang, Z. Y., Yu, J., and Cao, J. B. (2021). Complementary and catalytic roles of man-made VLF waves and natural plasma waves in the loss of radiation belt electrons. *J. Geophys. Res.: Space Phys.*, *126*(10), e2020JA028879. https://doi.org/10.1029/2020JA028879

Li, L. Y., Yu, J., Cao, J. B., Chen, L. J., Reeves, G. D., and Blake, J. B. (2022). Competitive influences of different plasma waves on the pitch angle distribution of energetic electrons inside and outside plasmasphere. *Geophys. Res. Lett.*, *49*(1), e2021GL096062. https://doi.org/10.1029/2021GL096062

Li, X. L., Baker, D. N., Temerin, M., Larson, D., Lin, R. P., Reeves, G. D., Looper, M., Kanekal, S. G., and Mewaldt, R. A. (1997). Are energetic electrons in the solar wind the source of the outer radiation belt?. *Geophys. Res. Lett.*, *24*(8), 923–926. https://doi.org/10.1029/97GL00543

Liu, B., Li, L. Y., Yu, J., and Cao, J. B. (2018). The effect of hot protons on magnetosonic waves inside and outside the plasmapause: new observations and theoretic results. *J. Geophys. Res.: Space Phys.*, *123*(1), 653–664. https://doi.org/10.1002/2017JA024676

Liu, K. J., Gary, S. P., and Winske, D. (2011). Excitation of magnetosonic waves in the terrestrial magnetosphere: particle-in-cell simulations. *J. Geophys. Res.*, *116*, A07212. https://doi.org/10.1029/2010JA016372

Liu, K. J., Winske, D., Gary, S. P., and Reeves, G. D. (2012). Relativistic electron scattering by large amplitude electromagnetic ion cyclotron waves: the role of phase bunching and trapping. *J. Geophys. Res.: Space Phys.*, *117*(A6), A06218. https://doi.org/10.1029/2011JA017476

Liu, Y. X. Z., Xiang, Z., Ni, B. B., Li, X. L., Zhang, K., Fu, S., Gu, X. D., Liu, J., and Cao, X. (2022). Quasi-trapped electron fluxes induced by NWC transmitter and CRAND: observations and simulations. *Geophys. Res. Lett.*, *49*(5), e2021GL097443. https://doi.org/10.1029/2021GL097443

Lou, Y. Q., Gu, X. D., Summers, D., Ni, B. B., Liu, K. J., Fu, S., Xiang, Z., Zou, Z. Y., Cao, X., … He, Y. (2018). Statistical distributions of dayside ECH waves observed by MMS. *Geophys. Res. Lett.*, *45*(23), 12730–12738. https://doi.org/10.1029/2018GL080125

Lou, Y. Q., Cao, X., Ni, B. B., Tu, W. C., Gu, X. D., Fu, S., Xiang, Z., and Ma, X. (2021). Diffuse auroral electron scattering by electrostatic electron cyclotron harmonic waves in the dayside magnetosphere. *Geophys. Res. Lett.*, *48*(5), e2020GL092208. https://doi.org/10.1029/2020GL092208

Lui, A. T. Y., Venkatesan, D., Anger, C. D., Akasofu, S. I., Heikkila, W. J., Winningham, J. D., and Burrows, J. R. (1977). Simultaneous observations of particle precipitations and auroral emissions by the Isis 2 satellite in the 19–24 MLT sector. *J. Geophys. Res.*, *82*(16), 2210–2226. https://doi.org/10.1029/JA082i016p02210

Lyons, L. R., and Thorne, R. M. (1973). Equilibrium structure of radiation belt electrons. *J. Geophys. Res.*, *78*(13), 2142–2149. https://doi.org/10.1029/ja078i013p02142

Ma, Q. L., Li, W., Chen, L., Thorne, R. M., Kletzing, C. A., Kurth, W. S., Hospodarsky, G. B., Reeves, G. D., Henderson, M. G., and Spence, H. E. (2014). The trapping of equatorial magnetosonic waves in the Earth's outer plasmasphere. *Geophys. Res. Lett.*, *41*(18), 6307–6313. https://doi.org/10.1002/2014GL061414

Ma, Q. L., Li, W., Thorne, R. M., Ni, B., Kletzing, C. A., Kurth, W. S., Hospodarsky, G. B., Reeves, G. D., Henderson, M. G., … Angelopoulos, V. (2015). Modeling inward diffusion and slow decay of energetic electrons in the Earth's outer radiation belt. *Geophys. Res. Lett.*, *42*(4), 987–995. https://doi.org/10.1002/2014GL062977

Ma, Q. L., Li, W., Thorne, R. M., Bortnik, J., Kletzing, C. A., Kurth, W. S., and Hospodarsky, G. B. (2016). Electron scattering by magnetosonic waves in the inner magnetosphere. *J. Geophys. Res.: Space Phys.*, *121*(1), 274–285. https://doi.org/10.1002/2015JA021992

Ma, X., Xiang, Z., Ni, B. B., Fu, S., Cao, X., Hua, M., Guo, D. Y., Guo, Y. J., Gu, X. D., … Zhu, Q. (2020). On the loss mechanisms of radiation belt electron dropouts during the 12 September 2014 geomagnetic storm. *Earth Planet. Phys.*, *4*(6), 598–610. https://doi.org/10.26464/epp2020060

Mauk, B. H., Fox, N. J., Kanekal, S. G., Kessel, R. L., Sibeck, D. G., and Ukhorskiy, A. (2013). Science objectives and rationale for the radiation belt storm probes mission. *Space Sci. Rev.*, *179*(1–4), 3–27. https://doi.org/10.1007/s11214-012-9908-y

Meng, C. I., Mauk, B., and McIlwain, C. E. (1979). Electron precipitation of evening diffuse aurora and its conjugate electron fluxes near the magnetospheric equator. *J. Geophys. Res.: Space Phys.*, *84*(A6), 2545–2558. https://doi.org/10.1029/ja084ia06p02545

Meredith, N. P., Horne, R. B., Glauert, S. A., Thorne, R. M., Summers, D., Albert, J. M., and Anderson, R. R. (2006). Energetic outer zone electron loss timescales during low geomagnetic activity. *J. Geophys. Res.: Space Phys.*, *111*(A5), A05212. https://doi.org/10.1029/2005JA011516

Meredith, N. P., Horne, R. B., Thorne, R. M., and Anderson, R. R. (2009). Survey of upper band chorus and ECH waves: implications for the diffuse aurora. *J. Geophys. Res.: Space Phys.*, *114*(A7), A07218. https://doi.org/10.1029/2009JA014230

Němec, F., Santolík, O., Gereová, K., Macúšová, E., De Conchy, Y., and Cornilleau-Wehrlin, N. (2005). Initial results of a survey of equatorial noise emissions observed by the Cluster spacecraft. *Planet. Space Sci.*, *53*(1–3), 291–298. https://doi.org/10.1016/j.pss.2004.09.055

Němec, F., Santolík, O., Gereová, K., Macúšová, E., Laakso, H., de Conchy, Y., Maksimovic, M., and Cornilleau-Wehrlin, N. (2006). Equatorial noise: statistical study of its localization and the derived number density. *Adv. Space Res.*, *37*(3), 610–616. https://doi.org/10.1016/j.asr.2005.03.025

Ni, B. B., Thorne, R. M., Shprits, Y. Y., and Bortnik, J. (2008). Resonant scattering of plasma sheet electrons by whistler-mode chorus: contribution to diffuse auroral precipitation. *Geophys. Res. Lett.*, *35*(11), L11106. https://doi.org/10.1029/2008GL034032

Ni, B. B., Thorne, R. M., Horne, R. B., Meredith, N. P., Shprits, Y. Y., Chen, L. J., and Li, W. (2011). Resonant scattering of plasma sheet electrons leading to

diffuse auroral precipitation: 1. Evaluation for electrostatic electron cyclotron harmonic waves. *J. Geophys. Res.*: *Space Phys.*, *116*(A4), A04218. https://doi.org/10.1029/2010JA016232

Ni, B. B., Bortnik, J., Thorne, R. M., Ma, Q. L., and Chen, L. J. (2013). Resonant scattering and resultant pitch angle evolution of relativistic electrons by plasmaspheric hiss. *J. Geophys. Res.*: *Space Phys.*, *118*(12), 7740–7751. https://doi.org/10.1002/2013JA019260

Ni, B. B., Cao, X., Zou, Z. Y., Zhou, C., Gu, X. D., Bortnik, J., Zhang, J. C., Fu, S., Zhao, Z. Y., … Xie, L. (2015). Resonant scattering of outer zone relativistic electrons by multiband EMIC waves and resultant electron loss time scales. *J. Geophys. Res.*: *Space Phys.*, *120*(9), 7357–7373. https://doi.org/10.1002/2015JA021466

Ni, B. B., Thorne, R. M., Zhang, X. J., Bortnik, J., Pu, Z. Y., Xie, L., Hu, Z. J., Han, D. S., Shi, R., … Gu, X. D. (2016). Origins of the Earth's diffuse auroral precipitation. *Space Sci. Rev.*, *200*(1–4), 205–259. https://doi.org/10.1007/s11214-016-0234-7

Ni, B. B., Hua, M., Zhou, R. X., Yi, J., and Fu, S. (2017a). Competition between outer zone electron scattering by plasmaspheric hiss and magnetosonic waves. *Geophys. Res. Lett.*, *44*(8), 3465–3474. https://doi.org/10.1002/2017GL072989

Ni, B. B., Gu, X. D., Fu, S., Xiang, Z., and Lou, Y. Q. (2017b). A statistical survey of electrostatic electron cyclotron harmonic waves based on THEMIS FFF wave data. *J. Geophys. Res.*: *Space Phys.*, *122*(3), 3342–3353. https://doi.org/10.1002/2016JA023433

Ni, B. B., Zou, Z. Y., Fu, S., Cao, X., Gu, X. D., and Xiang, Z. (2018). Resonant scattering of radiation belt electrons by off-equatorial magnetosonic waves. *Geophys. Res. Lett.*, *45*(3), 1228–1236. https://doi.org/10.1002/2017GL075788

Ni, B. B., Huang, H., Zhang, W. X., Gu, X. D., Zhao, H., Li, X. L., Baker, D., Fu, S., Xiang, Z., and Cao, X. (2019). Parametric sensitivity of the formation of reversed electron energy spectrum caused by plasmaspheric hiss. *Geophys. Res. Lett.*, *46*(8), 4134–4143. https://doi.org/10.1029/2019GL082032

Ni, B. B., Hua, M., Gu, X. D., Fu, S., Xiang, Z., Cao, X., and Ma, X. (2022). Artificial modification of Earth's radiation belts by ground-based very-low-frequency (VLF) transmitters. *Sci. China Earth Sci.*, *65*(3), 391–413. https://doi.org/10.1007/s11430-021-9850-7

Perraut, S., Roux, A., Robert, P., Gendrin, R., Sauvaud, J. A., Bosqued, J. M., Kremser, G., and Korth, A. (1982). A systematic study of ULF waves above F_{H+} from GEOS 1 and 2 measurements and their relationships with proton ring distributions. *J. Geophys. Res.*: *Space Phys.*, *87*(A8), 6219–6236. https://doi.org/10.1029/ja087ia08p06219

Reeves, G. D., McAdams, K. L., Friedel, R. H. W., and O'Brien, T. P. (2003). Acceleration and loss of relativistic electrons during geomagnetic storms. *Geophys. Res. Lett.*, *30*(10), 1529. https://doi.org/10.1029/2002gl016513

Roeder, J. L., and Koons, H. C. (1989). A survey of electron cyclotron waves in the magnetosphere and the diffuse auroral electron precipitation. *J. Geophys. Res.*: *Space Phys.*, *94*(A3), 2529–2541. https://doi.org/10.1029/ja094ia03p02529

Rönnmark, K. (1982). WHAMP: Waves in Homogeneous, Anisotropic, Multicomponent Plasmas. Kiruna, Sweden: Kiruna Geophysical Institute.

Russell, C. T., Holzer, R. E., and Smith, E. J. (1970). OGO 3 observations of ELF noise in the magnetosphere: 2. The nature of the equatorial noise. *J. Geophys. Res.*, *75*(4), 755–768. https://doi.org/10.1029/JA075i004p00755

Santolík, O., Pickett, J. S., Gurnett, D. A., Maksimovic, M., and Cornilleau-Wehrlin, N. (2002). Spatiotemporal variability and propagation of equatorial noise observed by Cluster. *J. Geophys. Res.*: *Space Phys.*, *107*(A12), 1495. https://doi.org/10.1029/2001JA009159

Santolík, O., Němec, F., Gereová, K., Macúšová, E., de Conchy, Y., and Cornilleau-Wehrlin, N. (2004). Systematic analysis of equatorial noise below the lower hybrid frequency. *Ann. Geophys.*, *22*(7), 2587–2595. https://doi.org/10.5194/angeo-22-2587-2004

Shprits, Y. Y., Subbotin, D., and Ni, B. B. (2009). Evolution of electron fluxes in the outer radiation belt computed with the VERB code. *J. Geophys. Res.*: *Space Phys.*, *114*(A11), A11209. https://doi.org/10.1029/2008JA013784

Shprits, Y. Y., Subbotin, D., Drozdov, A., Usanova, M. E., Kellerman, A., Orlova, K., Baker, D. N., Turner, D. L., and Kim, K. C. (2013). Unusual stable trapping of the ultrarelativistic electrons in the Van Allen radiation belts. *Nat. Phys.*, *9*(11), 699–703. https://doi.org/10.1038/nphys2760

Shprits, Y. Y. (2016). Estimation of bounce resonant scattering by fast magnetosonic waves. *Geophys. Res. Lett.*, *43*(3), 998–1006. https://doi.org/10.1002/2015GL066796

Su, Z. P., Liu, N. G., Zheng, H. N., Wang, Y. M., and Wang, S. (2018). Large-amplitude extremely low frequency hiss waves in plasmaspheric plumes. *Geophys. Res. Lett.*, *45*(2), 565–577. https://doi.org/10.1002/2017GL076754

Summers, D., Ma, C., Meredith, N. P., Horne, R. B., Thorne, R. M., and Anderson, R. R. (2004). Modeling outer-zone relativistic electron response to whistler-mode chorus activity during substorms. *J. Atmos. Solar-Terr. Phys.*, *66*(2), 133–146. https://doi.org/10.1016/j.jastp.2003.09.013

Summers, D., Ni, B. B., and Meredith, N. P. (2007a). Timescales for radiation belt electron acceleration and loss due to resonant wave–particle interactions: 1. Theory. *J. Geophys. Res.*: *Space Phys.*, *112*(A4), A04206. https://doi.org/10.1029/2006JA011801

Summers, D., Ni, B. B., and Meredith, N. P. (2007b). Timescales for radiation belt electron acceleration and loss due to resonant wave–particle interactions: 2. Evaluation for VLF chorus, ELF hiss, and electromagnetic ion cyclotron waves. *J. Geophys. Res.*: *Space Phys.*, *112*(A4), A04207. https://doi.org/10.1029/2006JA011993

Summers, D., Ni, B. B., Meredith, N. P., Horne, R. B., Thorne, R. M., Moldwin, M. B., and Anderson, R. R. (2008). Electron scattering by whistler-mode ELF hiss in plasmaspheric plumes. *J. Geophys. Res.*: *Space Phys.*, *113*(A4), A04219. https://doi.org/10.1029/2007JA012678

Tang, R. X., and Summers, D. (2019). Dependence of whistler mode chorus wave generation on the maximum linear growth rate. *J. Geophys. Res.*: *Space Phys.*, *124*(6), 4114–4124. https://doi.org/10.1029/2018JA026413

Teng, S. C., Ma, Q. L., and Tao, X. (2021). Simultaneous observations and combined effects of electromagnetic ion cyclotron waves and magnetosonic waves. *Geophys. Res. Lett.*, *48*(16), e2021GL093885. https://doi.org/10.1029/2021GL093885

Thorne, R. M., and Kennel, C. F. (1971). Relativistic electron precipitation during magnetic storm main phase. *J. Geophys. Res.*, *76*(19), 4446–4453. https://doi.org/10.1029/JA076i019p04446

Thorne, R. M., Smith, E. J., Burton, R. K., and Holzer, R. E. (1973). Plasmaspheric hiss. *J. Geophys. Res.*, *78*(10), 1581–1596. https://doi.org/10.1029/ja078i010p01581

Thorne, R. M., Church, S. R., and Gorney, D. J. (1979). On the origin of plasmaspheric hiss: the importance of wave propagation and the plasmapause. *J. Geophys. Res.*: *Space Phys.*, *84*(A9), 5241–5247. https://doi.org/10.1029/JA084iA09p05241

Thorne, R. M. (2010). Radiation belt dynamics: the importance of wave–particle interactions. *Geophys. Res. Lett.*, *37*(22), L22107. https://doi.org/10.1029/2010GL044990

Thorne, R. M., Li, W., Ni, B., Ma, Q., Bortnik, J., Baker, D. N., Spence, H. E., Reeves, G. D., Henderson, M. G., … Angelopoulos, V. (2013). Evolution and slow decay of an unusual narrow ring of relativistic electrons near L ~ 3.2 following the September 2012 magnetic storm. *Geophys. Res. Lett.*, *40*(14), 3507–3511. https://doi.org/10.1002/grl.50627

Usanova, M. E., Drozdov, A., Orlova, K., Mann, I. R., Shprits, Y., Robertson, M. T., Turner, D. L., Milling, D. K., Kale, A., … Wygant, J. (2014). Effect of EMIC waves on relativistic and ultrarelativistic electron populations: ground-based and Van Allen Probes observations. *Geophys. Res. Lett.*, *41*(5), 1375–1381. https://doi.org/10.1002/2013GL059024

Wang, J. L., Li, L. Y., and Yu, J. (2020). Statistical relationship between exohiss waves and plasmaspheric hiss. *Geophys. Res. Lett.*, *47*(5), e2020GL087023. https://doi.org/10.1029/2020GL087023

Xiang, Z., Tu, W. C., Ni, B. B., Henderson, M. G., and Cao, X. (2018). A statistical survey of radiation belt dropouts observed by Van Allen Probes. *Geophys. Res. Lett.*, *45*(16), 8035–8043. https://doi.org/10.1029/2018GL078907

Xiang, Z., Li, X. L., Temerin, M. A., Ni, B. B., Zhao, H., Zhang, K., and Khoo, L. Y. (2020a). On energetic electron dynamics during geomagnetic quiet times in Earth's inner radiation belt due to atmospheric collisional loss and

CRAND as a source. *J. Geophys. Res.*: *Space Phys.*, *125*(2), e2019JA027678. https://doi.org/10.1029/2019ja027678

Xiang, Z., Li, X. L., Ni, B. B., Temerin, M. A., Zhao, H., Zhang, K., and Khoo, L.Y. (2020b). Dynamics of energetic electrons in the slot region during geomagnetically quiet times: losses due to wave–particle interactions versus a source from cosmic ray albedo neutron decay (CRAND). *J. Geophys. Res.*: *Space Phys.*, *125*(9), e2020JA028042. https://doi.org/10.1029/2020ja028042

Xiang, Z., Li, X. L., Kapali, S., Gannon, J., Ni, B. B., Zhao, H., Zhang, K., and Khoo, L. Y. (2021). Modeling the dynamics of radiation belt electrons with source and loss driven by the solar wind. *J. Geophys. Res.*: *Space Phys.*, *126*(6), e2020JA028988. https://doi.org/10.1029/2020JA028988

Xiao, F. L., Su, Z. P., Zheng, H. N., and Wang, S. (2009). Modeling of outer radiation belt electrons by multidimensional diffusion process. *J. Geophys. Res.*: *Space Phys.*, *114*(A3), A03201. https://doi.org/10.1029/2008JA013580

Xiao, F. L., Zhou, Q. H., He, Z. G., Yang, C., He, Y. H., and Tang, L. J. (2013). Magnetosonic wave instability by proton ring distributions: simultaneous data and modeling. *J. Geophys. Res.*: *Space Phys.*, *118*(7), 4053–4058. https://doi.org/10.1002/jgra.50401

Xiao, F. L., Yang, C., Su, Z. P., Zhou, Q. H., He, Z. G., He, Y. H., Baker, D. N., Spence, H. E., Funsten, H. O., and Blake, J. B. (2015). Wave-driven butterfly distribution of Van Allen belt relativistic electrons. *Nat. Commun.*, *6*, 8590. https://doi.org/10.1038/ncomms9590

Xue, Z. X., Yuan, Z. G., Yu, X. D., Huang, S. Y. and Qiao, Z. (2021). Formation of the mass density peak at the magnetospheric equator triggered by EMIC waves. *Earth Planet. Phys.*, *5*(1), 32–41. https://doi.org/10.26464/epp2021008

Yang, L., Li, L. Y., Cao, J. B., and Yu, J. (2022). Statistical properties of whistler-mode hiss waves in the inner radiation belt. *J. Geophys. Res.*: *Space Phys.*, *127*(5), e2022JA030444. https://doi.org/10.1029/2022JA030444

Yu, J., Li, L. Y., Cao, J. B., Yuan, Z. G., Reeves, G. D., Baker, D. N., Blake, J. B., and Spence, H. (2015). Multiple loss processes of relativistic electrons outside the heart of outer radiation belt during a storm sudden commencement. *J. Geophys. Res.*: *Space Phys.*, *120*(12), 10275–10288. https://doi.org/10.1002/2015JA021460

Yu, J., Li, L. Y., Cao, J. B., Chen, L., Wang, J., and Yang, J. (2017). Propagation characteristics of plasmaspheric hiss: Van Allen Probe observations and global empirical models. *J. Geophys. Res.*: *Space Phys.*, *122*(4), 4156–4167. https://doi.org/10.1002/2016JA023372

Yu, J., Wang, J., Li, L. Y., Cui, J., Cao, J. B., and He, Z. G. (2020). Electron diffusion by coexisting plasmaspheric hiss and chorus waves: multisatellite observations and simulations. *Geophys. Res. Lett.*, *47*(15), e2020GL088753. https://doi.org/10.1029/2020GL088753

Zhang, X. J., Chen, L. J., Artemyev, A. V., Angelopoulos, V., and Liu, X. (2019). Periodic excitation of chorus and ECH waves modulated by ultralow frequency compressions. *J. Geophys. Res.*: *Space Phys.*, *124*(11), 8535–8550. https://doi.org/10.1029/2019JA027201

Zhou, R. X., Fu, S., Gu, X. D., Ma, X., Ni, B. B., Yi, J., Guo, Y. J., Guo, D. Y., Jiao, L. H., … Wang, X. Y. (2022). Combined scattering of concurrent unusual high-frequency EMIC waves and MS waves on radiation belt electrons. *Geophys. Res. Lett.*, *49*(13), e2022GL098378. https://doi.org/10.1029/2022GL098378

Zhu, H., Su, Z. P., Xiao, F. L., Zheng, H. N., Wang, Y. M., Shen, C., Xian, T., Wang, S., Kletzing, C. A., … Baker, D. N. (2015). Plasmatrough exohiss waves observed by Van Allen Probes: evidence for leakage from plasmasphere and resonant scattering of radiation belt electrons. *Geophys. Res. Lett.*, *42*(4), 1012–1019. https://doi.org/10.1002/2014GL062964